Commissioning and first results from the new 2 × 100 TW laser at the WIS

View Online   Export Citation   CrossMark

E. Kroupp,[1,a] S. Tata,[1] Y. Wan[1] D. Levy[1] S. Smartsev[1] E. Y. Levine[1] O. Seemann[1] M. Adelberg,[1]
R. Piliposian,[1] T. Queller[1] E. Segre,[1] K. Ta Phuoc[2] M. Kozlova[3,4] and V. Malka[1]

AFFILIATIONS

[1] Faculty of Physics, Weizmann Institute of Science, Rehovot 7610001, Israel
[2] Laboratoire d'Optique Appliquée, Ecole polytechnique—ENSTA—CNRS—Institut Polytechnique de Paris, Palaiseau, France
[3] Institute of Physics, CAS, ELI Beamlines, Na Slovance 2, 182 21 Prague 8, Czech Republic
[4] Institute of Plasma Physics, CAS, Za Slovankou 3, 182 21 Prague 8, Czech Republic

[a] Author to whom correspondence should be addressed: eyal.kroupp@weizmann.ac.il

ABSTRACT

At the Weizmann Institute of Science, a new high-power-laser laboratory has been established that is dedicated to the fundamental aspects of laser–matter interaction in the relativistic regime and aimed at developing compact laser-plasma accelerators for delivering high-brightness beams of electrons, ions, and x rays. The HIGGINS laser system delivers two independent 100 TW beams and an additional probe beam, and this paper describes its commissioning and presents the very first results for particle and radiation beam delivery.

I. INTRODUCTION

Laser–matter interaction in the relativistic regime has opened a new area of research that is rich in fundamental processes and promises of applications, and the laser-plasma acceleration that results from this interaction allows the production of beams of electrons, ions, and x rays. The Weizmann Institute of Science (WIS) facility—which delivers two independent powerful laser beams that can interact in the same target chamber—has been built to perform unique pump–probe experiments of matter irradiated by laser beams at relativistic intensity, and depending on the parameters, the plasma can be probed by an x-ray, proton, or electron beam.

Laser-wakefield electron acceleration[1] has developed rapidly over the past four decades, with the capability of generating high-energy (from hundreds of megaelectronvolts to several giga-electronvolts) electron sources in short distances from millimeters to centimeters.[2–7] For modern 100 TW lasers, the focused intensity reaches a relativistic scale and drives a nonlinear plasma wake with acceleration gradients reaching 100 GV/m. In this regime, electrons are easily trapped and accelerated to very high energies inside the plasma wake,[8,9] and this self-injection process is the most common and straightforward mechanism used in nonlinear wakefield acceleration for electrons. This regime has been discussed

thoroughly in the literature and provides a benchmark for the performance of our laser system and target chamber. Motivated by its many societal applications,[9] laser-plasma acceleration of electrons was the first scheme that we addressed, and we report the results herein.

Betatron x-ray radiation from relativistic laser–plasma interaction has great potential in modern x-ray applications, and its femtosecond duration, broadband spectra, and micrometer source size are essential advantages for x-ray absorption spectroscopy,[10] x-ray diffraction,[11] and others.[12–16] A betatron x-ray source is analogous to a synchrotron but with millimeter-scale electron acceleration length.[17,18] Here again, the intense femtosecond laser beam focused onto the underdense plasma pushes electrons away from its path and drives an ion cavity—also called a bubble—in its wake. This cavity acts simultaneously as an electron accelerator and a wiggler. Trapped electrons are accelerated in the longitudinal direction and are wiggled in the transverse direction by strong electromagnetic fields, resulting in a slalom-like trajectory. In a typical case, electrons reach energies of a few hundred megaelectronvolts and oscillate with a longitudinal period of a few hundred micrometers and a transverse amplitude of a few micrometers. At relativistic energies, wiggling electrons emit x-ray photons, known as betatron radiation.[19]

The interaction of the laser beam with a dense target—such as a thin foil that is opaque to the laser light—permits efficient conversion of the laser energy into hot electrons,[20,21] with temperatures that can easily reach a few megaelectronvolts at the considered laser intensities of the order of 10^{20} W/cm². Those electrons produced at the vacuum–foil interface of the irradiated target propagate through the foil, and upon exiting its rear surface they form a negatively charged sheath with a thickness of the order of the local Debye length, giving rise to huge electrostatic fields that can easily reach several megavolts per micrometer with a 100 TW laser system. These fields readily ionize the contaminants on the surface of the foil, and the ionized hydrogen contaminants (protons) quickly rush to the vacuum and are accelerated to the highest momenta among all ions because of their largest charge-to-mass ratio.[22]

At the WIS, the new HIGGINS high-power-laser laboratory is dedicated to exploring the fundamental aspects of the relativistic regime, developing particle and radiation beams, and exploring the most relevant applications. Opened in 2016, this fully equipped laboratory was ready to host the laser system in 2018 and to commission the laser-plasma accelerators soon after. Herein, we describe the laser system and measured laser beam parameters in Sec. II, then we present the very first results for electron acceleration (Sec. III A), x-ray betatron radiation (Sec. III B), and ion acceleration (Sec. III C), before concluding in Sec. IV.

II. THE LASER SYSTEM

The WIS laser system was conceived by WIS and Thales teams and built by the Thales Group (France). The laser was designed to deliver two beams of up to 2.7 J and 27 fs duration, each at a 1 Hz

repetition rate, and we have implemented a 30 mJ 45 fs probe beam. The choice of two independent 100 TW laser beams sets the ground for performing a wide range of pump–probe experiments, for example by probing the plasmas created by the pump laser beam with an electron, proton, or x-ray beam produced by the second laser beam. The first pump–probe experiment has been performed, in which the relativistic plasma waves were probed by an ultra-short (duration of a few femtoseconds) and relativistic (up to 500 MeV) electron beam.

Figure 1 shows a block diagram of the laser system, which is based on Ti:sapphire as the gain medium. Pulses from a 75 MHz oscillator are stretched and amplified in a regenerative amplifier and are then recompressed and filtered with a cross-polarized wave (XPW) system based on two BaF₂ crystals; the XPW improves the temporal contrast of the femtosecond laser pulses by between four and five orders of magnitude.[23] The pulses are stretched again to ~300 ps and are amplified by only multi-pass amplifiers to maintain the temporal contrast. After stretching, a Dazzler is added to control the spectral amplitude and phase, providing additional control to obtain the best compression after amplification. Another Pockels cell acting as a pulse cleaner is also installed to improve the nanosecond temporal contrast by four orders of magnitude. The pulses are then amplified by three different multi-pass amplifiers. Between the stretcher, preamplifier, and first amplifier, two Faraday isolators are used to protect the system from back reflections.

The first multi-pass amplifier (Preamplifier) increases the pulse energy from ~4 μJ to 30 mJ, and the following amplifier (AMP1) increases it to 1.2 J. Next, a 5% reflection from a glass wedge is added to pick off the probe. The final multi-pass amplifier (AMP2) is then
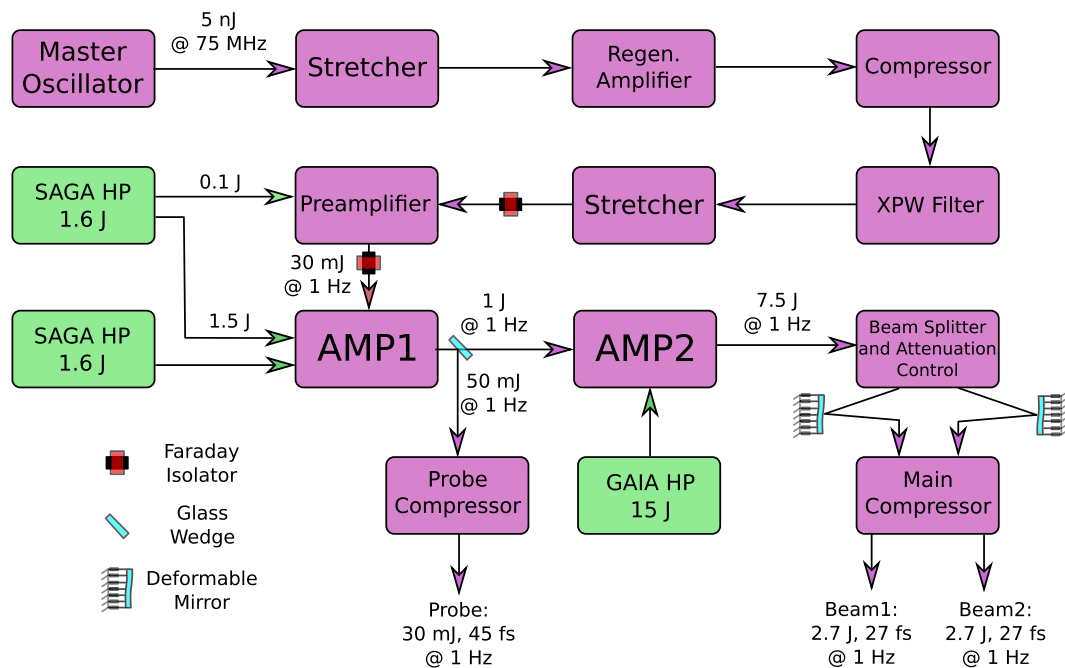

FIG. 1. Block diagram of Weizmann Institute of Science (WIS) laser system. Pump units are shown in green.

used to increase the energy to 7.5 J. The repetition rate is determined by the large-aperture frequency-doubled Nd:YAG pump laser that provides 15 J at 532 nm, operating at 1 Hz.

The beam is then split into two beams with energy up to 3.7 J each before compression. The energy stability was measured to be 0.7% rms with a sequence of 20 shots. Each beamline contains a set of $\lambda/2$ waveplates and polarizers to control and attenuate the energy down to a few millijoules. Further in the beamline, low surface irregularity ($\lambda/5$) neutral density transmission filters were added, allowing accurate measurement of the focal spot and other diagnostics with full laser amplification. Each beamline also contains a deformable mirror of 90 mm diameter located before the compressor chamber. Figures 2(a) and 2(b) show the laser room and a deformable mirror.

During an experiment, pulses are selected by a rapidly rotating pulse selector, triggered with reference to a software-based "ARM" button to allow the laser pulse to pass into the compressor. The pulse selector is implemented as a ceramic diffuser [Fig. 2(c)] for each beam to allow pulse selection at full power; this allows the laser to be in thermal equilibrium during the experiment, thereby enhancing the shot-to-shot stability.

The whole laser system (excluding the transport line and the compressor) is completely decoupled from the building and sits on eight concrete foundation pillars that run ~10 m underground. Mechanical decoupling, together with temperature and humidity control systems, make the laser extremely stable. Because the laser beams (two main beams and the probe beam) are sourced from the same oscillator, the time jitter among them in the target

chamber—located ~10 m from the beam splitter—is no more than 10 fs, originating from micrometer-scale vibrations of the reflective optics along the beam line and measured by pump–probe experiments that will be published independently. All the target chambers and the transport line are in vacuum, and all the optics and devices
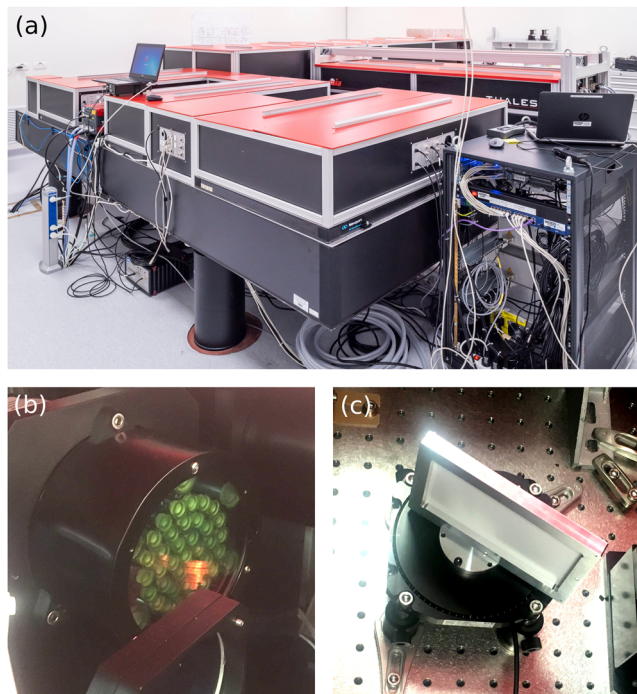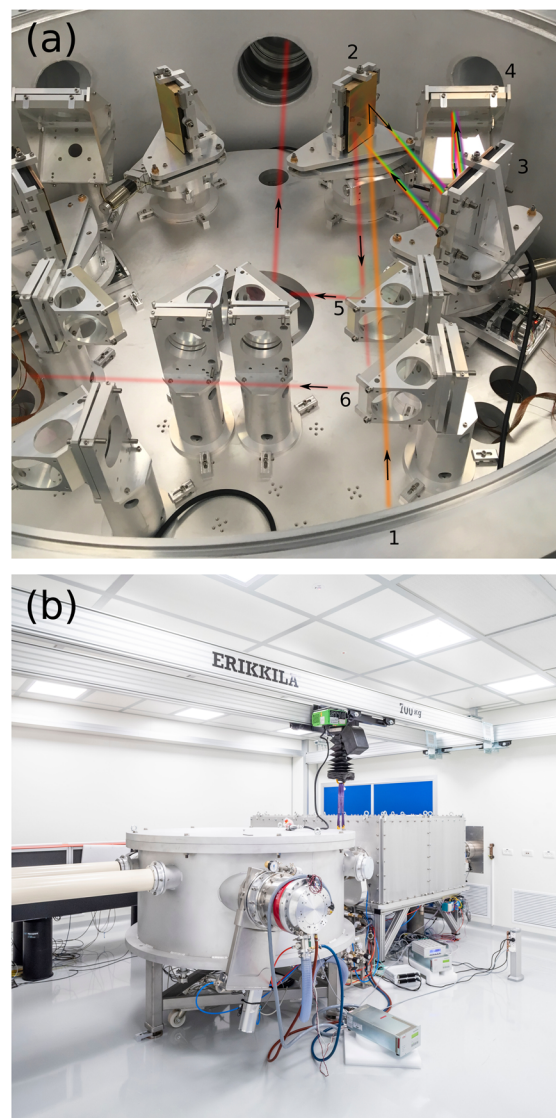

FIG. 3. (a) Interior of compressor chamber, with a sketch depicting the path of one of the two IR beams. The uncompressed beam (orange in the image) enters near (1) and reflects off the tops of the first and second gratings (2 and 3, respectively), becoming spatially chirped (rainbow pattern). It is shifted vertically down by the periscope (4), reflects off the bottoms of the second and first gratings (3 and 2, respectively), thereby completing the compression (red in the image). Most of the beam (5) is sent to the experimental chamber, and a small part is leaked (6) and sent to the diagnostics bench. The second high-power beam traverses a similar path in the left half of the compressor chamber. (b) Compressor (front, round) and deformable mirror (rear, square) chambers inside the clean room. For scale, the external diameter of the compressor chamber is ~1.7 m.

FIG. 2. (a) Photograph of WIS laser system. (b) Deformable mirror for one of the beams. (c) Ceramic diffuser used as a pulse selector.

FIG. 4. General view of experimental hall showing the target chambers: electron/x-ray-beam chamber (left); ion-beam chamber (right).

that are in vacuum are set on base plates; for better beam stability, these base plates are decoupled from the vacuum chambers.

The compressor chamber shown in Fig. 3(a) hosts two independent compressors for the two high-energy beams. Each of the main compressors has a pair of gratings (130 × 200 mm² and 210 × 200 mm²). The efficiency of each compressor is ~70%.

The compressor chamber and an adjacent chamber (that will contain additional deformable mirrors but currently contains a third independent compressor for the probe beam) sit in a clean room in between the laser room and the experimental hall [see Fig. 3(b)]. After compression, the beams are reflected by partially transparent mirrors, and the leaking beams are transported onto a diagnostic table where beam profile, energy, spectrum, pulse duration, phase-front correction, and pulse contrast can be measured online during experiments. Each main beam's spatial profile before and after the main compression is a quasi-top hat with 55 mm diameter and 75 mm edges; the probe beam is 25 mm in diameter.

The beams then reach the experimental hall, which hosts the target chambers (see Fig. 4) where ions, electrons, and x rays are produced. In the experimental hall, each beam can be transported to either target chamber by a set of dielectric mirrors placed in three turn-boxes.

Each target chamber has a red alignment laser transmitted into the beamline through the dielectric mirrors reflecting the 800 nm laser. The alignment laser is a cw laser with a visible 660 nm wavelength (hereinafter, we refer to it as the red laser, as opposed to the main IR laser); see Fig. 5. The main design challenge was expanding the red beam by more than a factor of 55 while maintaining a spatial phase front of sufficient quality, given the imperfect beam front of the laser diode. This challenge was overcome by using a spatial filter inside a diffraction-limited Keplerian beam expander.
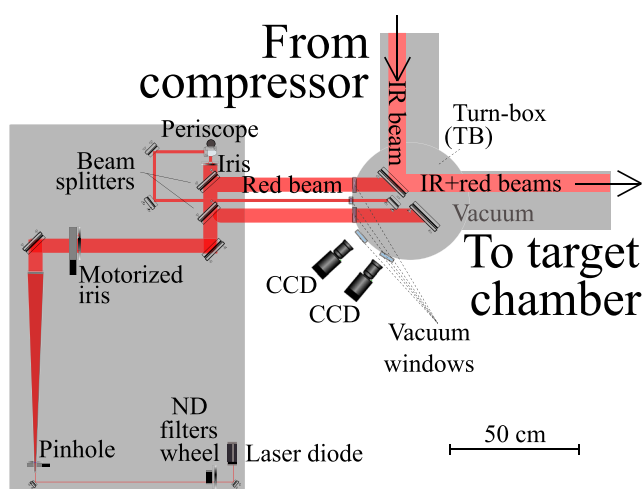

FIG. 5. Simplified setup of alignment (red) laser and relationship with main (IR) laser.
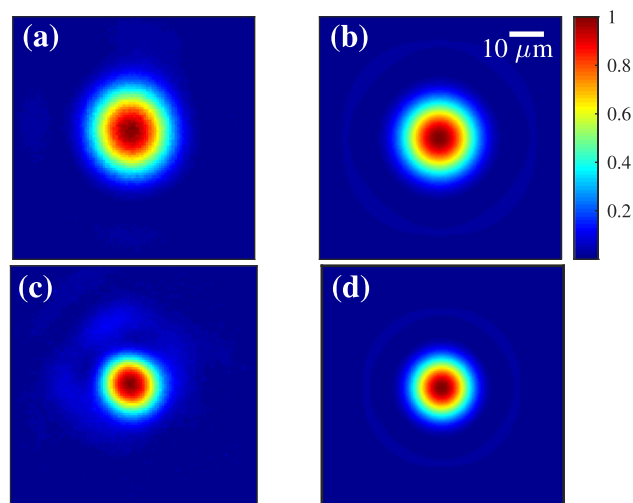

FIG. 6. Focal spots of red alignment and main IR laser beams: (a) measured and (b) simulated red (660 nm) focal spots with $f/25$; (c) measured and (d) simulated main IR laser focal spots with $f/17$.
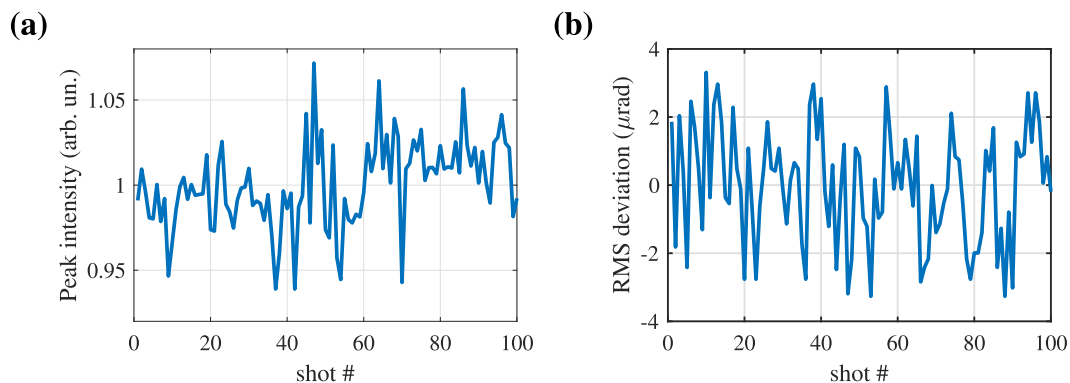
(a) **(b)**

FIG. 7. Focal-spot stability over 100 consecutive shots: (a) peak intensity fluctuations vs shot number; (b) RMS deviation vs shot number.

The red laser that emulates the IR laser is used to assemble and align all of the optical elements inside the target chamber easily and comfortably. Once the experiment is aligned with the red laser, the IR laser is superimposed precisely onto it by using the motorized mirrors in the turn-boxes before the target chamber.

The focal-spot stability was measured at full laser amplification, which was later attenuated down to nanojoule energy pulses, focused by an $f/16$ off-axis parabolic mirror (OAP). The focal spot was then imaged by a microscope objective on a CCD camera, and the spatial phase of the IR laser beam was corrected using a deformable mirror. Typical measured focal spots of the red and IR lasers are shown in Figs. 6(a) and 6(c), respectively; corresponding spots simulated by propagating beams with a perfect (flat) phase to the far-field via FFT using the Zemax software are shown in Figs. 6(b) and 6(d), respectively. As can be seen, the measured focal spots are close to being diffraction-limited.

The statistical analysis of the data in Fig. 7 shows $\sigma_{intensity} \approx 2.5\%$ for the mean peak intensity fluctuations and $\sigma_{spatial} \approx 1.7\ \mu$rad for the spatial fluctuations. The normalized

peak intensity of one arbitrary unit for the IR laser in Figs. 6(c) and 7(a) corresponds to 2.7×10^{19} W/cm^2, assuming 2.3 J of energy in the pulse at the target when operated at full power after all transport losses. This energy value was estimated as follows: the energy was measured before the compressor at full power, then the value was adjusted considering the laser transport line and compressor transmissions to the target, which were measured independently with low-energy pulses.

We measured the temporal profile of both beams by means of self-referenced spectral interference.[24] Just before focusing, we directed a small central part of the attenuated beam into a Fastlite Wizzler device. As shown in Fig. 8(a), we have an approximately flat spectral phase for both beams, leading to nearly transform-limited pulses in time. This is shown in Fig. 8(b) with a FWHM of 25 and 27 fs for beam 1 and 2, respectively. The pulse contrast at picosecond time scale was evaluated using a third-order autocorrelator[25] (Tundra device by Ultrafast Innovations). As can be seen in Fig. 8(c), the contrast spans nearly ten orders of magnitude.
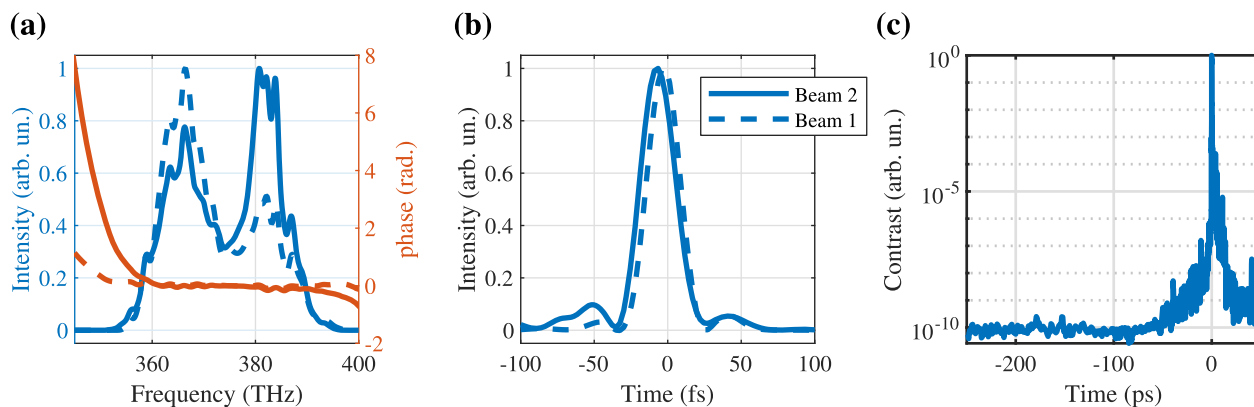
(a) **(b)** **(c)**

FIG. 8. Self-referenced spectral interference and third-order autocorrelator measurements: (a) measured spectral intensity and phase with (b) temporal reconstruction of pulse intensity; (c) laser contrast plotted on logarithmic scale.

III. FIRST EXPERIMENTAL RESULTS

A. Electron acceleration

For the commissioning of the electron acceleration, we performed a laser-wakefield experiment with a supersonic gas jet as the target. We chose a 0.5–3 mm converging–diverging supersonic gas nozzle puffed with pure helium, and the laser was synchronized to arrive at the gas target after 7 ms, ensuring a steady flow from the nozzle. A typical gas density profile generated by this system with a backing pressure of 10 bars is shown in Fig. 9. Figure 9(a) shows two Abel-inverted density profiles from both sides of the symmetry axis, and Fig. 9(b) shows the density profile along the laser propagation axis 1 mm above the nozzle.

The laser beam was focused by an OAP with a 1 m focal length to a spot size of 18 μm (FWHM). The enclosed laser energy, within $1/e^2$ in intensity, was estimated at ~60%, corresponding to a peak intensity of 10^{19} W/cm². The intense laser beam fully ionized the helium into plasma and drove a very strong nonlinear wakefield; electrons were injected continuously when they moved close to the end of the wake and were accelerated efficiently. The diagnostic for the electron spectra comprised (i) a permanent dipole magnet (10 cm long, magnetic field of 1 T) that was placed ~19 cm from the gas jet and (ii) a 25.5-cm-long calibrated[26] Lanex scintillator screen placed after it to intercept electrons in the energy range of 40–700 MeV. The emitted light signal was imaged onto a 16 bits CCD camera behind a 546 ± 40 nm interference filter.

Under optimal conditions of a backing pressure of 10 bars, reproducible, low-divergence, high-energy electrons were generated stably. As an example, Fig. 10 presents a series of 20 consecutive shots that shows a stable electron source with maximum energy of more than 500 MeV and 90 ± 20 pC charge above 50 MeV. An rms beam divergence of 3.0 ± 0.7 mrad and beam pointing fluctuations of ~4 mrad were achieved. The relatively large energy spread can be attributed to continuous self-injection in the nonlinear plasma wake.

B. Betatron x-ray radiation

For the commissioning of the betatron beam, a dedicated experiment was run. The high-power laser was focused onto the
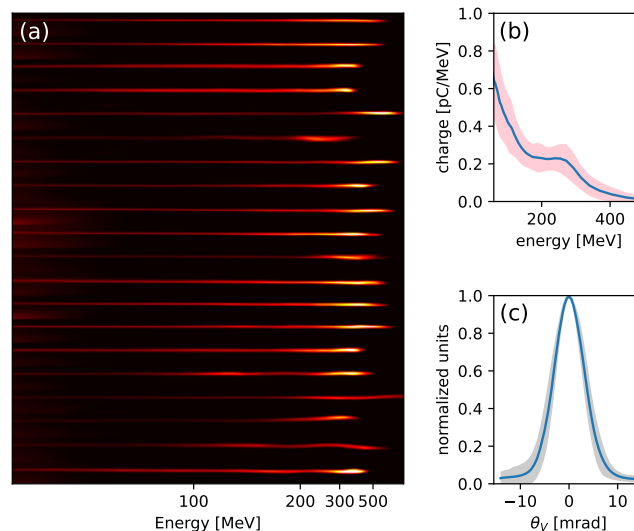

FIG. 10. Twenty consecutive shots: (a) raw data on electron spectrometer; (b) averaged electron spectra (solid blue curve) with shot-to-shot stability (red shaded region); (c) averaged electron vertical divergence (solid blue curve) with shot-to-shot stability (gray shaded area).

gas jet emitted from the same 3 mm supersonic nozzle that was described in Sec. III A, but this time with a 98% helium and 2% nitrogen gas mixture.

The accelerated electrons wiggled in the intense transverse electric field that resulted from the charge separation initiated by the transverse ponderomotive force of the laser, thereby emitting betatron x-ray radiation in a collimated beam along the laser direction. Further along the acceleration axis, we placed a fixed dipole magnet, deflecting the accelerated electrons and separating them from the betatron photons. On the other hand of the magnet, we placed a Ross-filter system[27,28] (an assembly of several foils of various metallic elements and thicknesses), and after it a Lanex screen to convert
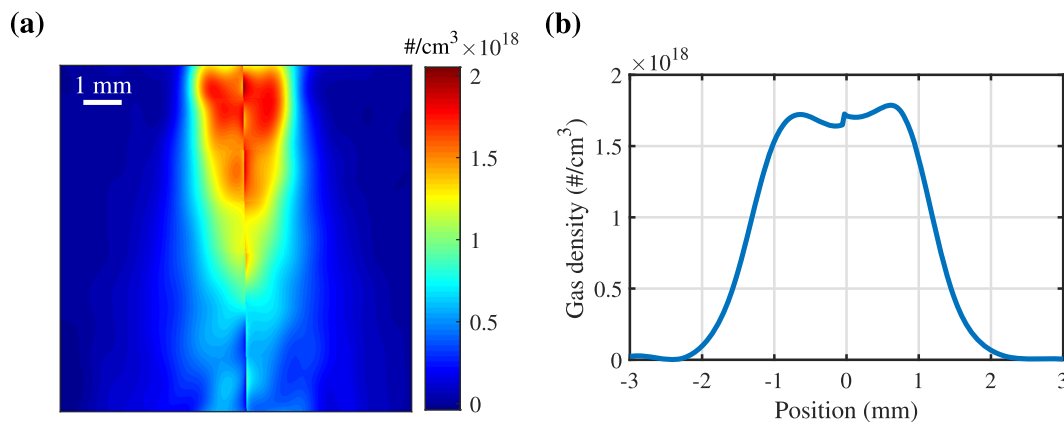

FIG. 9. Measured gas density profile using a 0.5–3 mm converging–diverging supersonic nozzle with a backing pressure of 10 bars: (a) Abel-inverted gas density profile showing inversion from both sides of the symmetry axis; (b) gas density profile as a function of position along the laser axis 1 mm above the nozzle.

the x-ray photons into visible photons that were collected by a CCD camera.

As the betatron beam passed through the Ross-filter foils, it was attenuated differently according to each element's transmission spectrum (see Fig. 11), allowing reconstruction of the betatron x-ray spectrum based on brightness differences among the different regions.

To reconstruct the x-ray spectrum, the Ross-filter image was fitted to a 2D Gaussian distribution, with the image regions corresponding to the different metals multiplied by possible absorption coefficients. The best fit gave both the beam shape (aspect ratio and tilt angle of the elliptical beam, divergence, and pointing angle) and the absorption ratios at each part of the image. We then found the spectrum that best fitted the measured absorption coefficients: for any given candidate spectrum, and given the known metals comprising the Ross-filter system, we calculated the expected absorption coefficients for that spectrum and found the one with the best match. For our fit, we use a synchrotron radiation function parameterized by a critical (cutoff) energy E_c.

During the spectrum reconstruction, several uncertainty sources should be considered: the CCD pixel noise, affecting the brightness estimation of the image regions; the metal-foil thickness uncertainty, which can lead to errors in modeling the absorption; and the Lanex response uncertainty. Of these, the metal-foil thickness uncertainty contributes the most to the uncertainty in the beam energy.

Figure 12(a) shows the analysis results for the above example betatron signal in terms of the reconstructed spectrum and the uncertainty region due to the aforementioned factors. The critical energy value for this beam is estimated as $E_c = 9.7$ keV. Figure 12(b) shows the data from 26 shots, showing that the estimated E_c is distributed approximately normally, with a mean value of 9.8 keV and a standard deviation of 0.65 keV.

C. Ion acceleration

The commissioning of laser ion acceleration was achieved using thin metallic foils as targets. Ions were accelerated using the well-known and robust mechanism of target normal sheath acceleration.[20] The laser beam was focused by an $f/3$ OAP onto thin (2–5 μm) stainless-steel, aluminum, or titanium foils,
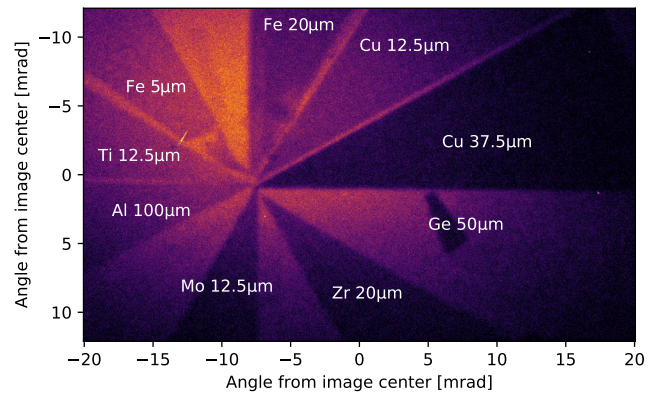

FIG. 11. Scintillator screen image showing betatron beam (centered in red-orange area) and absorption caused by various sector-shaped Ross-filter metal foils. The elements and thicknesses used are annotated on the corresponding regions.

and hundreds of shots were carried out during the scanning of various experimental conditions. To measure the energy distribution of the accelerated ions, two diagnostics were used in two separate experiments, i.e., a 2D scintillator-based profiler[29,30] and a Thomson parabola spectrometer (TPS), the aim being to validate these diagnostics for the commissioning of the laboratory.

The 2D scintillator profiler has an aluminum mask with nine circular cuts with logarithmic spacing thicknesses and placed in a grid formation (120 μm to 2.115 mm). Only protons above the cutoff energy for the local mask thickness pass through and imprint a signal on the scintillator screen located immediately thereafter. A fit to an exponential energy distribution with a cutoff was carried out using published data for the proton stopping power in aluminum. This technique allows for 2D energy spectrum measurements. A typical image of the scintillator results and derived intensity curves for two specific angles are shown in Fig. 13, where it can be seen that the higher-energy components of the beam are collimated more sharply. Accelerated protons reaching up to 14 MeV were measured at 5°, while a cutoff energy of 10 MeV was measured at 13°. These values
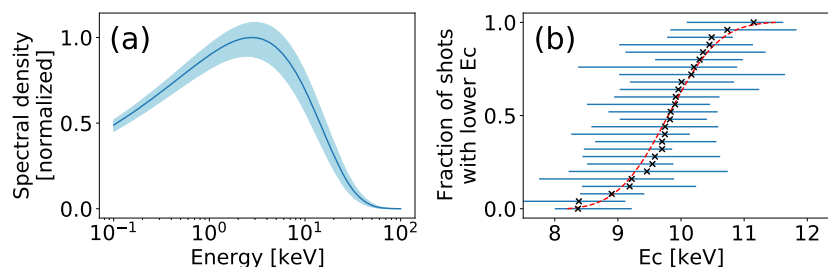

FIG. 12. (a) Betatron radiation spectrum reconstructed from information in Ross-filter image. The estimated critical energy is $E_c = 9.7$ keV, and the shaded region represents the uncertainty in this parameter, which is (8.6, 10.6) keV. (b) Plot showing for each energy value the fraction of 26 shots that had a lower critical energy than this value [empirical cumulative distribution function, (eCDF)]. Shown are the estimated E_c values of the shots (black crosses) with their error bars (blue solid lines), along with the CDF of a normal distribution with a mean value of 9.8 keV and a standard deviation of 0.65 keV (red dashed line).
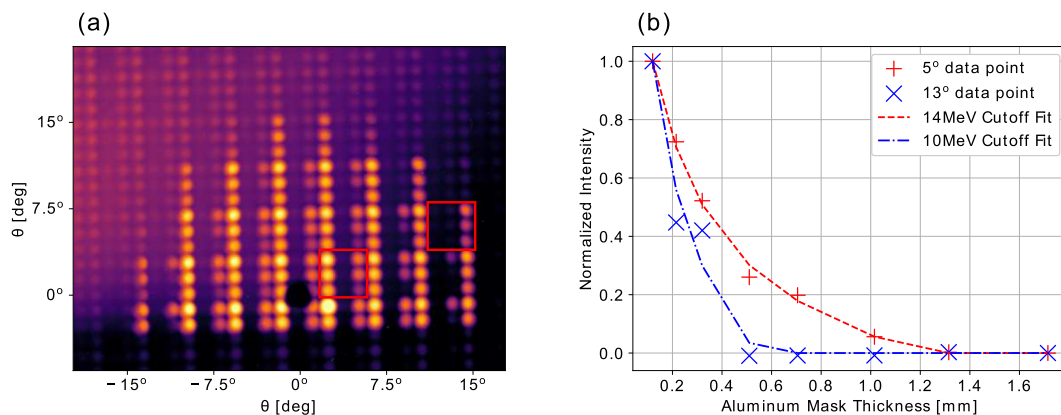
FIG. 13. (a) Image of 2D scintillator intensity map in logarithmic scale. The circular bright spots are an imprint of the aluminum mask with nine different thicknesses. A complex angular energy dependence is observed. The bright top-left part is due to electrons deflected by a magnet; they exhibit a different relative intensity response. The bottom part is blocked by a thick object. The red rectangles mark two different-angle points for further analysis. The target foil itself—2 μm of Ti—is oriented at 45° to the laser. (b) Normalized intensity curves at 5° and 13° angles extracted from the image. The dashed lines are the fitted expected responses for an exponential distribution of protons. The best fit for the beam at 5° gives a cutoff energy of 14 MeV, while that at 13° gives 10 MeV, showing that the more energetic components of the beam are collimated more sharply.

are comparable to energies obtained with laser systems of similar power.[31]

The TPS was designed and built for detecting accelerated charged particles; see Fig. 14. The particles enter the TPS through a 0.5 mm pinhole and are deflected by magnetic and electrostatic fields. After deflection, the particles travel in free space and impinge upon a microchannel plate coupled to a phosphor screen. The resulting parabolic-like curves on the screen are imaged by a CCD camera.
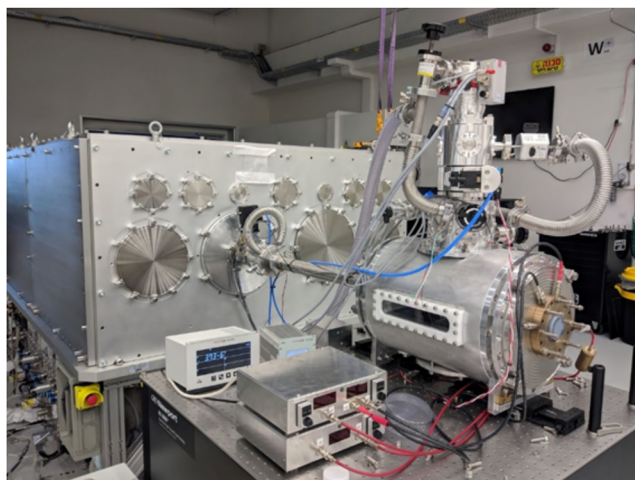

FIG. 14. The ~0.5 m long Thomson parabola spectrometer (TPS) chamber (front right) connected to the target chamber (rear left) via a ~1 m vacuum tube. On the left side of the TPS chamber is the window for electron detection, and on its back side is the microchannel-plate detector. A 70 l/s turbo pump is placed on top of the TPS chamber, where on the optical table are shown the high-voltage power supplies and vacuum meter.

Each curve corresponds to positive ions of a different charge-to-mass ratio. Particles with higher initial velocity are deflected less than are particles with lower initial velocity because of the shorter interaction time with the deflecting fields. Knowing the values of the electric and magnetic fields, each point on the measured curves can be mapped to an initial velocity (or kinetic energy) of the corresponding ion species.

The magnetic field is generated by two permanent magnets, and the average magnitude of the on-axis field measures 0.38 T over 5 cm. The electrostatic field is generated by two oppositely charged copper plates that are 5 cm long, and the magnitude of the field can be varied between zero and 5 kV/cm. The free propagation distance (the distance between the electric-field plates and the microchannel plate), which determines the energy detection range of the detector, can be varied by sliding the magnets and electrodes on a rail inside the TPS chamber.

The TPS design also allows for detection of electrons that are deflected by the magnets, in this case through a slit in the holder. Using a scintillator screen such as a Lanex, it is possible to measure the energy spectrum of electrons emitted from the target. The measurable energy range varies according to the magnet position. We implemented this option in a single experimental campaign with a structured target, and no runaway electrons were detected, presumably because of their divergence, which makes the signal be below the detection threshold.

A typical ion measurement is shown in Fig. 15. The proton energy spectrum is shown after subtraction of a background curve located parallel with and below the signal curve. The spatial extent of the ion signal on the detector (the curve width) is the principal source of error in estimating peak ion energies. This quantity is a function of the pinhole diameter and its distance from the source and to the detector, and it is measured to be 1 mm. The relative error E_{kin}/E_{kin} is also a function of the maximum measured energy E_{kin}, where for our geometry we find $\Delta E_{kin}/E_{kin} \approx 0.01 \left(\frac{E_{kin}}{\text{MeV}} \right)^{1/2}$.
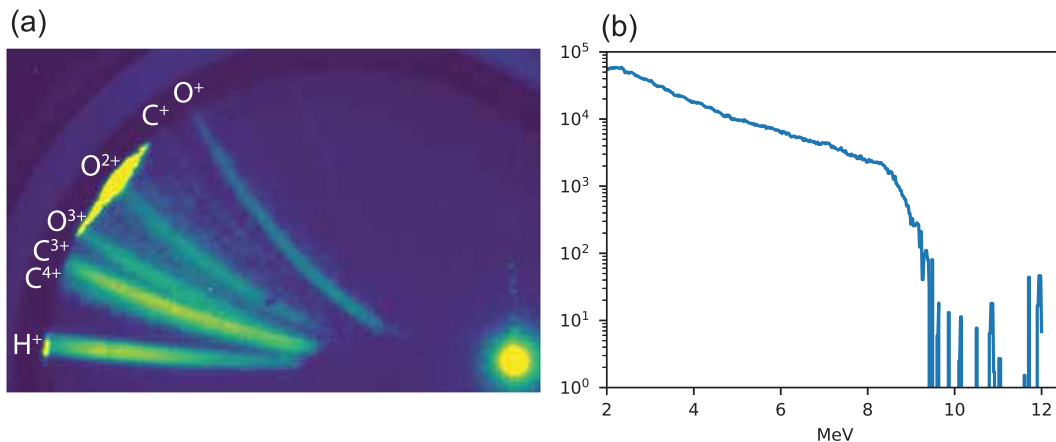
FIG. 15. (a) A typical Thomson parabola image. The target was a 5-μm stainless-steel foil that was nearly normal to the laser, and the various curves correspond to different ion species. (b) The proton energy spectrum extracted from (a), showing a cutoff energy of 9.4 ± 0.3 MeV for this shot.

IV. CONCLUSION

The new dual 100 TW HIGGINS laser system has delivered all the requested parameters for performing innovative experiments in the relativistic regime of laser–matter interaction. The first three experiments that followed the commissioning of the laser system succeeded in delivering beams of electrons, ions, and x rays. Overall, the laser system and the experimental infrastructure including the beam transport, targets, and diagnostics work perfectly, and therefore the system is now ready for the actual exploration of novel concepts and exciting applications.

AUTHOR DECLARATIONS

Conflict of Interest

The authors have no conflicts to disclose.

DATA AVAILABILITY

The datasets generated during and/or analysed during the current study are available from the corresponding author on reasonable request.

REFERENCES

[1] T. Tajima and J. M. Dawson, "Laser electron accelerator," Phys. Rev. Lett. **43**, 267–270 (1979).

[2] J. Faure, Y. Glinec, A. Pukhov, S. Kiselev, S. Gordienko, E. Lefebvre, J.-P. Rousseau, F. Burgy, and V. Malka, "A laser-plasma accelerator producing monoenergetic electron beams," Nature **431**, 541–544 (2004).

[3] C. G. R. Geddes, C. Toth, J. Van Tilborg, E. Esarey, C. B. Schroeder, D. Bruhwiler, C. Nieter, J. Cary, and W. P. Leemans, "High-quality electron beams from a laser wakefield accelerator using plasma-channel guiding," Nature **431**, 538–541 (2004).

[4] S. P. D. Mangles, C. D. Murphy, Z. Najmudin, A. G. R. Thomas, J. L. Collier, A. E. Dangor, E. J. Divall, P. S. Foster, J. G. Gallacher, C. J. Hooker, D. A. Jaroszynski, A. J. Langley, W. B. Mori, P. A. Norreys, F. S. Tsung, R. Viskup, B. R. Walton, and K. Krushelnick, "Monoenergetic beams of relativistic electrons from intense laser-plasma interactions," Nature **431**, 535–538 (2004).

[5] H. T. Kim, K. H. Pae, H. J. Cha, I. J. Kim, T. J. Yu, J. H. Sung, S. K. Lee, T. M. Jeong, and J. Lee, "Enhancement of electron energy to the multi-GeV regime by a dual-stage laser-wakefield accelerator pumped by petawatt laser pulses," Phys. Rev. Lett. **111**, 165002 (2013).

[6] A. J. Gonsalves, K. Nakamura, J. Daniels, C. Benedetti, C. Pieronek, T. C. H. de Raadt, S. Steinke, J. H. Bin, S. S. Bulanov, J. van Tilborg, C. G. R. Geddes, C. B. Schroeder, C. Tóth, E. Esarey, K. Swanson, L. Fan-Chiang, G. Bagdasarov, N. Bobrova, V. Gasilov, G. Korn, P. Sasorov, and W. P. Leemans, "Petawatt laser guiding and electron beam acceleration to 8 GeV in a laser-heated capillary discharge waveguide," Phys. Rev. Lett. **122**, 084801 (2019).

[7] A. Pukhov and J. Meyer-ter-Vehn, "Laser wake field acceleration: The highly non-linear broken-wave regime," Appl. Phys. B **74**, 355–361 (2002).

[8] W. Lu, M. Tzoufras, C. Joshi, F. S. Tsung, W. B. Mori, J. Vieira, R. A. Fonseca, and L. O. Silva, "Generating multi-GeV electron bunches using single stage laser wakefield acceleration in a 3D nonlinear regime," Phys. Rev. Spec. Top.-Accel. Beams **10**, 061301 (2007).

[9] V. Malka, J. Faure, Y. A. Gauduel, E. Lefebvre, A. Rousse, and K. T. Phuoc, "Principles and applications of compact laser–plasma accelerators," Nat. Phys. **4**, 447–453 (2008).

[10] B. Mahieu, N. Jourdain, K. Ta Phuoc, F. Dorchies, J.-P. Goddet, A. Lifschitz, P. Renaudin, and L. Lecherbourg, "Probing warm dense matter using femtosecond X-ray absorption spectroscopy with a laser-produced betatron source," Nat. Commun. **9**, 3276 (2018).

[11] K. Ta Phuoc, R. Fitour, A. Tafzi, T. Garl, N. Artemiev, R. Shah, F. Albert, D. Boschetto, A. Rousse, D.-E. Kim, A. Pukhov, V. Seredov, and I. Kostyukov, "Demonstration of the ultrafast nature of laser produced betatron radiation," Phys. Plasmas **14**, 080701 (2007).

[12] S. Fourmaux, S. Corde, K. T. Phuoc, P. Lassonde, G. Lebrun, S. Payeur, F. Martin, S. Sebban, V. Malka, A. Rousse, and J. C. Kieffer, "Single shot phase contrast imaging using laser-produced betatron x-ray beams," Opt. Lett. **36**, 2426–2428 (2011).

[13] J. Wenz, S. Schleede, K. Khrennikov, M. Bech, P. Thibault, M. Heigoldt, F. Pfeiffer, and S. Karsch, "Quantitative X-ray phase-contrast microtomography from a compact laser-driven betatron source," Nat. Commun. **6**, 7568 (2015).

[14] J. M. Cole, J. C. Wood, N. C. Lopes, K. Poder, R. L. Abel, S. Alatabi, J. S. J. Bryant, A. Jin, S. Kneip, K. Mecseki, D. R. Symes, S. P. D. Mangles, and Z. Najmudin, "Laser-wakefield accelerators as hard x-ray sources for 3D medical imaging of human bone," Sci. Rep. **5**, 13244 (2015).

[15] S. Corde, C. Thaury, K. T. Phuoc, A. Lifschitz, G. Lambert, J. Faure, O. Lundh, E. Benveniste, A. Ben-Ismail, L. Arantchuk, A. Marciniak, A. Stordeur, P. Brijesh, A. Rousse, A. Specka, and V. Malka, "Mapping the x-ray emission region in a laser-plasma accelerator," Phys. Rev. Lett. **107**, 215004 (2011).

[16] M. C. Downer, R. Zgadzaj, A. Debus, U. Schramm, and M. C. Kaluza, "Diagnostics for plasma-based electron accelerators," Rev. Mod. Phys. **90**, 035002 (2018).

[17] S. Kiselev, A. Pukhov, and I. Kostyukov, "X-ray generation in strongly nonlinear plasma waves," Phys. Rev. Lett. **93**, 135004 (2004).

[18] A. Rousse, K. T. Phuoc, R. Shah, A. Pukhov, E. Lefebvre, V. Malka, S. Kiselev, F. Burgy, J.-P. Rousseau, D. Umstadter, and D. Hulin, "Production of a keV x-ray beam from synchrotron radiation in relativistic laser-plasma interaction," Phys. Rev. Lett. **93**, 135005 (2004).

[19] S. Corde, K. Ta Phuoc, G. Lambert, R. Fitour, V. Malka, A. Rousse, A. Beck, and E. Lefebvre, "Femtosecond x rays from laser-plasma accelerators," Rev. Mod. Phys. **85**, 1–48 (2013).

[20] S. C. Wilks, A. B. Langdon, T. E. Cowan, M. Roth, M. Singh, S. Hatchett, M. H. Key, D. Pennington, A. MacKinnon, and R. A. Snavely, "Energetic proton generation in ultra-intense laser–solid interactions," Phys. Plasmas **8**, 542–549 (2001).

[21] T. Ceccotti, A. Lévy, H. Popescu, F. Réau, P. D'Oliveira, P. Monot, J. P. Geindre, E. Lefebvre, and P. Martin, "Proton acceleration with high-intensity ultrahigh-contrast laser pulses," Phys. Rev. Let. **99**, 185002 (2007).

[22] J. Fuchs, P. Antici, E. d'Humières, E. Lefebvre, M. Borghesi, E. Brambrink, C. A. Cecchetti, M. Kaluza, V. Malka, M. Manclossi, S. Meyroneinc, P. Mora, J. Schreiber, T. Toncian, H. Pépin, and P. Audebert, "Laser-driven proton scaling laws and new paths towards energy increase," Nat. Phys. **2**, 48–54 (2006).

[23] A. Jullien, J.-P. Rousseau, B. Mercier, L. Antonucci, O. Albert, G. Chériaux, S. Kourtev, N. Minkovski, and S. M. Saltiel, "Highly efficient nonlinear filter for femtosecond pulse contrast enhancement and pulse shortening," Opt. Lett. **33**, 2353–2355 (2008).

[24] T. Oksenhendler, S. Coudreau, N. Forget, V. Crozatier, S. Grabielle, R. Herzog, O. Gobert, and D. Kaplan, "Self-referenced spectral interferometry," Appl. Phys. B **99**, 7–12 (2010).

[25] V. A. Schanz, F. Wagner, M. Roth, and V. Bagnoud, "Noise reduction in third order cross-correlation by angle optimization of the interacting beams," Opt. Express **25**, 9252–9261 (2017).

[26] T. Kurz, J. P. Couperus, J. M. Krämer, H. Ding, S. Kuschel, A. Köhler, O. Zarini, D. Hollatz, D. Schinkel, R. D'Arcy, J.-P. Schwinkendorf, J. Osterhoff, A. Irman, U. Schramm, and S. Karsch, "Calibration and cross-laboratory implementation of scintillating screens for electron bunch charge determination," Rev. Sci. Instrum. **89**, 093303 (2018).

[27] P. A. Ross, "Minutes of the Oakland meeting, June 17, 1926," Phys. Rev. **28**, 425–430 (1926).

[28] P. A. Ross, "A new method of spectroscopy for faint x-radiations," J. Opt. Soc. Am. **16**, 433–437 (1928).

[29] J. Metzkes, K. Zeil, S. D. Kraft, L. Karsch, M. Sobiella, M. Rehwald, L. Obst, H.-P. Schlenvoigt, and U. Schramm, "An online, energy-resolving beam profile detector for laser-driven proton beams," Rev. Sci. Instrum. **87**, 083310 (2016).

[30] N. P. Dover, M. Nishiuchi, M. Sakaki, M. A. Alkhimova, A. Y. Faenov, Y. Fukuda, H. Kiriyama, A. Kon, K. Kondo, K. Nishitani, K. Ogura, T. A. Pikuz, A. S. Pirozhkov, A. Sagisaka, M. Kando, and K. Kondo, "Scintillator-based transverse proton beam profiler for laser-plasma ion sources," Rev. Sci. Instrum. **88**, 073304 (2017).

[31] K. Zeil, S. D. Kraft, S. Bock, M. Bussmann, T. E. Cowan, T. Kluge, J. Metzkes, T. Richter, R. Sauerbrey, and U. Schramm, "The scaling of proton energies in ultrashort pulse laser plasma acceleration," New J. Phys. **12**, 045015 (2010).